JOURNAL OF THEORETICAL AND APPLIED MECHANICS
63, 1, pp. 177-195, Warsaw 2025
https://doi.org/10.15632/jtam-pl/194881

RESPONSE ANALYSIS AND CONTROL OF COMPOSITE THIN PLATE WITH PIEZOELECTRIC ACTUATORS BY FINITE ELEMENT METHOD

Trieu Long Vo, Dai Duc Mai, Long Nhut-Phi Nguyen
HCMC University of Technology and Education (HCMUTE), Ho Chi Minh City, Vietnam
Nhan Nguyen Dang
Cao Thang Technical College (CTCT), Ho Chi Minh City, Vietnam
Son Hoai Nguyen
Nguyen Tat Thanh University (NTTU), Ho Chi Minh City, Vietnam
corresponding author Son Hoai Nguyen, email: sonnh@ntt.edu.vn

This paper presents the shape deformation of a thin plate coupled to piezoelectric actuators and sensors analyzed using the finite element method (FEM). The coupling effects between electric and mechanical properties of the piezoelectric material draw attention to potential applications, such as actuators, sensors, etc. The proposed method is analyzed and evaluated, and its effectiveness is proven. Firstly, a rectangular piezoelectric actuator with three symmetrically bonded sensors is used. Secondly, it is applied to control the swimming pool diving board. Combination of FEM and LQR active control algorithms through numerical simulation results shows changing shape and position of the piezoelectric patch which makes premises for an experiment and production.

Keywords: piezoelectric actuator, piezoelectric sensor, thin plate theory, coupling effect, Finite Element Method (FEM), LQR

1. Introduction

In recent years, many studies about the behavior of piezoelectric structures have been researched and investigated. It is a key standout among them that piezo materials with some advantages such as the quick response, low energy consumption, and high linearity, have been studied and developed for a decade (Uchino, 2010; Lumentut and Howard, 2014; Bhalla *et al.*, 2017; Wei *et al.*, 2018; Chen *et al.*, 2020). The piezoelectric device is interesting in structure engineering, applying shape control, reducing noise and controuing stability of structures (Uchino, 1986; Wang and Shen, 1998; Adriaens *et al.*, 2000; Chen etal, 2016; Chen *et al.*, 2018; Reddy, 1999). For example, Saravanos and Heyliger (1999) covered important information about theories, analytical approaches, computational models, and numerical solutions for analyzing laminates and structures in piezoelectric actuator or sensor systems. Jafferis *et al.* (2016) used multilayer laminated piezoelectric bending actuators in the design and manufacturing to achieve optimum efficiency and power density. Moreover, Bailey and Hubbard (1985) presented that vibration of a cantilever beam was controlled by an adaptative law using a PFDV film as the actuator. A two-dimensional piezoelectric material bonded on the surface with a simply supported plate were revealed by Dimitriadis *et al.* (1991). Benjeddou *et al.* (2000) described the shear actuation mechanism, which offerred several promising features for the use of piezoelectric ceramics. Luo and Tong developed a finite element model to analyze and simulate twisting and bending shape control using an orthotropic piezoelectric actuator (Luo and Tong, 2006). Huang and Sun (2006) used piezoelectricity in an actuator to control dynamic adaption with an anisotropic elastic structure. Additionally, the effect of piezoelectric arrays symmetrically attached to opposite

plate surfaces in continuous operation of a composite structure was evaluated by Dimitriadis *et al.* (1991), Crawley and Luis (1987). Phung-Van *et al.* (2013) proposed the cell-based smoothed discrete shear gap approach (CS-FEM-DSG3) to improve static vibration of a fan and introduced a dynamic control model for composite plates integrated into piezoelectric sensors and actuators. Furthermore, Hoa *et al.* (2018) used the cell-based smoothed discrete shear gap method for evaluating free and static vibration of laminated composite shells. Moretti and Silva (2019) presented the use of the Topology optimization method (TOM) in designing a bi-material piezoelectric actuator (BPEA), which was capable of eliminating vibration with the active velocity feedback control (AVFC). By reading velocity state variables in the time domain, the AVFC shows its influence on the system structural damping. This study uses Newmark's time-integration method to yield dynamic response results for the rectangular four-noded finite element (FE) analysis (this method uses physical and adjoint systems because the coupling formula is extremely important in sensitivity analysis). The authors use the gradient-based optimization method when applying a mechanical load instantaneously to minimize the displacement energy output, which is determined at a predefined BPA's DOF (degree of freedom). Cao *et al.* (2020) used the classical laminated plate theory and the Fourier transformation to analyze and control actively vibration of thin-constrained composite plates and damping characteristics with dual piezoelectric layers. The study results about natural frequencies and losses of a damped composite plate bound with two piezoelectric layers were found through 3D electric potential equations. Trojanowski and Wiciak (2020) presented numerical simulation results (using ANSYS software) of the influence of sensor-actuator size on the plate performance. Two piezoelectric actuators were placed on a steel plate: one to stimulate the plate and one (a standard actuator or a sensor-actuator with different shapes and sizes) to reduce plate vibrations. The results of numerical analysis show agreement with the objective function: the minimum value of the sum of the displacement vectors of n nodes. Karegar *et al.* (2021) presented the dynamic analysis of a concrete frame with a smart layer under earthquake load conditions. The article evaluated the influence of external voltage, plate thickness, boundary conditions, geometric parameters of the frame, and damping of the structure on the seismic displacement of the frame. The authors used the Grey Wolf (GW) optimization algorithm and hyperbolic shear deformation (HSD) theory to model the flat frame and Hamilton's principle to derive the governing equation of the frame. Based on that relationship, the numerical methods of differential quadrature and Newark's one were used to study this concrete frame response. Gohery *et al.* (2022) developed a Levi-type analytical solution procedure to describe the static and dynamic deformation response of smart laminated rectangular composite plates supported under the influence of inclined piezoelectric actuators with some excitation frequency. Latrache and Menasri (2022) used piezoelectric actuators and sensor pads to actively control vibration of the classical laminated plate with embedded piezoelectric patches. The authors built a coupled finite element (FE) model with mechanical and electrical degrees of freedom based on the first-order shear deformation (FSD) theory and Hamilton's principle. At the same time, based on the independent mode space control techniques, the authors designed the Linear Quadratic Regulator (LQR) controller to limit the system vibration. Her and Chen (2022) proposed a theoretical model predicting the vibration response of a laminate composite (LC) plate to control the shape and suppress vibrations through piezoelectric actuators. The analytical solution to that vibration response was derived using the composite mechanics and plate theory. Numerical simulation results using the finite element method (FEM) through ANSYS software were very well compared with the proposed model.

In this article, the shape deformation of the plate bonded to piezoelectric actuators and sensors is investigated by the FEM. Based on the Kirchhoff plate model, a finite element analysis has been evolved for the analysis of smart composite structures with a piezoelectric material. Two cases are implemented to prove the effectiveness of the proposed method in improving the reliability of the model algorithm. The tasks are done as follows. Firstly, a rectangular piezo-

electric actuator with symmetrically bonded three sensors is considered. In the second case, the piezoactuator of the injector is implemented and controlled by the diving board in diving sports. The simulated results verify the behavior of plate drive modules with changes in the piezo patch position and composite plate fiber direction. The article also analyzes and compares classical control strategies (constant amplitude and constant velocity feedback). Classical techniques have the advantages of avoiding the necessity of digital control, reducing time delays, and providing stability. A major limitation of the LQR is that all states must be measured when generating control.

2. Structure modeling

As mentioned in (Reddy, 1999), the assumptions are considered as follows: (1) the piezoelectric layers are perfectly bonded to each other, (2) the behavior of linear elastic materials is a disadvantage of the presented formula, (3) based on the Kirchhoff hypothesis (thin plate), the horizontal normal remains straight after deforming and rotating, ensuring that it is always perpendicular to the mid-surface.

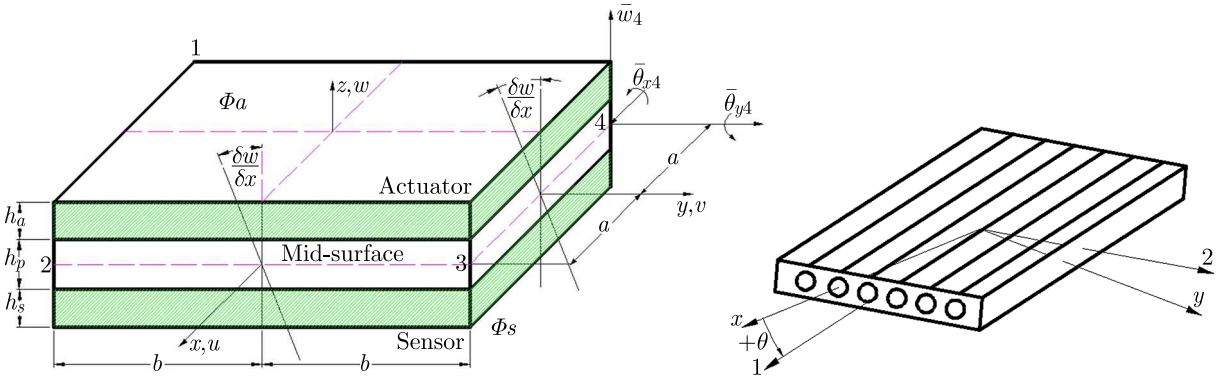

Fig. 1. A laminated finite element coordinate system with the integrated piezoelectric material (left) and the fiber direction in local and global coordinate systems (right)

Based on the Kirchhoff hypothesis, the displacement fields in u, v and w variables can be obtained as follows (Reddy, 1999)

$$u = -z\frac{\partial w}{\partial x} \qquad v = -z\frac{\partial w}{\partial y} \qquad w = w(x,y) \tag{2.1}$$

where $Oxyz$ is the Descartes coordinate system, located at the mid-surface. Additionally, u and v are displacements of the x and y-axes, while the transverse displacement w follows (or aka deflection) in the z-axis

$$\boldsymbol{\varepsilon} = [\varepsilon_x, \varepsilon_y, \gamma_{xy}] = -z\left[\frac{\partial^2 w}{\partial x^2}, \frac{\partial^2 w}{\partial y^2}, \frac{\partial^2 w}{\partial x \partial y}\right]^{\mathrm{T}} \tag{2.2}$$

The relation between the plane stress σ and strain ε of the isotropic material is denoted by

$$\boldsymbol{\sigma} = \mathbf{D}\boldsymbol{\varepsilon} \tag{2.3}$$

where

$$\boldsymbol{\sigma} = [\sigma_x, \sigma_x, \tau_{xy}]^{\mathrm{T}} \qquad \mathbf{D} = \frac{E_p}{1-v^2}\begin{bmatrix} 1 & v & 0 \\ v & 1 & 0 \\ 0 & 0 & (1-v)/2 \end{bmatrix} \tag{2.4}$$

and σ, ε, ν, E_p are stress, strain field, Poisson's ratio, and Young's modulus, respectively.

The composite material panels are made of many consecutive layers in which the direction of the fiber or basic direction is different. The relationship between stress and strain in the global system is as follows

$$\begin{bmatrix}\sigma_x\\ \sigma_y\\ \tau_{xy}\end{bmatrix} = \mathbf{Q}' \begin{bmatrix}\varepsilon_x\\ \varepsilon_y\\ \gamma_{xy}\end{bmatrix} \begin{bmatrix}Q'_{11} & Q'_{12} & Q'_{16}\\ Q'_{12} & Q'_{22} & Q'_{26}\\ Q'_{16} & Q'_{26} & Q'_{66}\end{bmatrix} \begin{bmatrix}\varepsilon_x\\ \varepsilon_y\\ \gamma_{xy}\end{bmatrix} \tag{2.5}$$

where

$$\begin{aligned}
Q;_{11} &= Q_{11}\cos^4\theta + 2(Q_{12}+2Q_{66})\sin^2\theta\cos^2\theta + Q_{22}\sin^4\theta\\
Q'_{12} &= (Q_{11}+Q_{22}-4Q_{66})\sin^2\theta\cos^2\theta + Q_{12}\sin^4\theta\cos^4\theta\\
Q'_{22} &= Q_{11}\sin^4\theta + 2(Q_{12}+2Q_{66})\sin^2\theta\cos^2\theta + Q_{22}\cos^4\theta\\
Q'_{16} &= (Q_{11}-Q_{12}-2Q_{66})\sin\theta\cos^3\theta + (Q_{12}-Q_{22}+2Q_{66})\sin^3\theta\cos\theta\\
Q'_{26} &= (Q_{11}-Q_{12}-2Q_{66})\sin^3\theta\cos\theta + (Q_{12}-Q_{22}+2Q_{66})\sin\theta\cos^3\theta\\
Q'_{66} &= (Q_{11}+Q_{12}-2Q_{12}-2Q_{66})\sin^2\theta\cos^2\theta + Q_{66}(\sin^4\theta+\cos^4\theta)
\end{aligned} \tag{2.6}$$

In fact, $\mathbf{Q}'$ is a complete matrix indicating that the shear strain γ_{xy} in the (x,y) plane is associated with the normal strain ε_x, ε_y. This behavior is called the shear strain and shear strain long form.

Similarly

$$\begin{bmatrix}\varepsilon_x\\ \varepsilon_y\\ \tau_{xy}\end{bmatrix} = \mathbf{S}' \begin{bmatrix}\sigma_x\\ \sigma_y\\ \tau_{xy}\end{bmatrix} \begin{bmatrix}S'_{11} & S'_{12} & S'_{16}\\ S'_{12} & S'_{22} & S'_{26}\\ S'_{16} & S'_{26} & S'_{66}\end{bmatrix} \begin{bmatrix}\sigma_x\\ \sigma_y\\ \tau_{xy}\end{bmatrix} \tag{2.7}$$

Layer softness composition $\mathbf{S}' = \{S'_{ij}\}$ with $i,j = 1,2$

$$\mathbf{S}' = \mathbf{T}_{\varepsilon}^{-1}\mathbf{S}\mathbf{T} \tag{2.8}$$

where

$$\begin{aligned}
S'_{11} &= S_{11}\cos^4\theta + S_{22}\sin^4\theta + 2(S_{12}+2S_{66})\cos^2\theta\sin^2\theta\\
S'_{12} &= S_{12}(\cos^4\theta+\sin^4\theta) + (S_{11}+S_{22}-S_{66})\cos^2\theta\sin^2\theta\\
S'_{16} &= (S_{11}-S_{12}-2S_{66})\sin\theta\cos^3\theta + (S_{12}-S_{22}+2S_{66})\sin^3\theta\cos\theta\\
S'_{22} &= S_{11}\sin^4\theta + S_{22}\cos^4\theta + (2S_{12}+S_{66})\sin^2\theta\cos^2\theta\\
S'_{26} &= (2S_{11}-2S_{12}-S_{66})\cos\theta\sin^3\theta + (2S_{12}+S_{66}-2S_{22})\cos^3\theta\sin\theta\\
S'_{66} &= S_{66}(\cos^4\theta+\sin^4\theta) + 2(S_{11}+S_{22}-4S_{12}-S_{66})\sin^2\theta\cos^2\theta
\end{aligned} \tag{2.9}$$

with

$$\begin{aligned}
S_{11} &= \frac{1}{E_1} \qquad S_{12} = -\frac{\nu_{12}}{E_2} \qquad S_{21} = -\frac{\nu_{21}}{E_2}\\
S_{22} &= \frac{1}{E_2} \qquad S_{66} = \frac{1}{G_{12}} \qquad S_{16} = S_{26} = S_{61} = S_{62} = 0
\end{aligned} \tag{2.10}$$

where E_1, E_2, ν_{12}, ν_{21}, G_{12} are Young's elastic modulus, Poisson's coefficients, and the corresponding in-plane shear elastic modulus (Fig. 1, right).

Based on the original plate theory in the finite element analysis, considering a four-node rectangular plate bending element is developed (Bailey and Hubbard, 1985). Figure 2 shows the

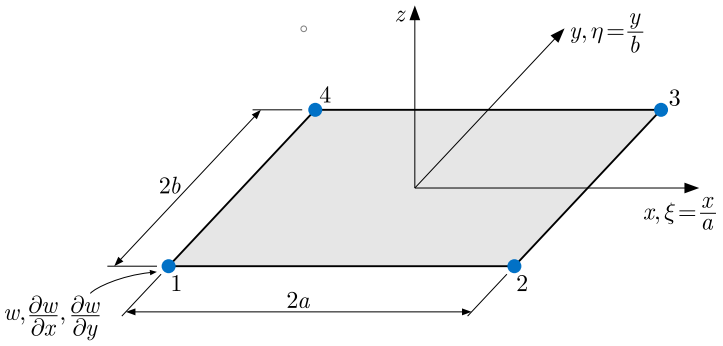

Fig. 2. 3-DOF (degrees of freedom) of the rectangular element per node

DOF (degrees of freedom) number of each node of the element: w displacement in the z direction, $\theta_x = \partial w/\partial x$ rotation around the x-axis, and $\theta_y = \partial w/\partial y$ rotation around the y-axis.

Based on the Pascal triangle law, the interpolation function is selected. The displacement w at an arbitrary point in the element is as follows

$$\begin{aligned} w(x_i, y_i) = {} & c_1 + c_2 x_i + c_3 y_i + c_4 x_i^2 + c_5 y_i x_i + c_6 y_i^2 + c_7 x_i^3 \\ & + c_8 x_i^2 y_i + c_8 x_i y_i^2 + c_{10} y_i^3 + c_{11} x_i^3 y_i + c_{12} x_i y_i^3 \end{aligned} \tag{2.11}$$

where $(i = 1, 2, 3, 4)$

$$x_1 = x_4 = -a \qquad x_2 = x_3 = a \qquad y_1 = y_2 = -b \qquad y_3 = y_4 = b \tag{2.12}$$

The transverse displacement field w is expressed by $w = \mathbf{P}^T \mathbf{c}$, where

$$\begin{aligned} \mathbf{P} &= [1, x, y, x^2, xy, y^2, x^3, x^2 y, xy^2, y^3, x^3 y, xy^3]^{\mathrm{T}} \\ \mathbf{c} &= [c_1, c_2, c_3, c_4, c_5, c_6, c_7, c_8, c_9, c_{10}, c_{11}, c_{12}] \end{aligned} \tag{2.13}$$

In the rectangular element, the node displacement field vector $\mathbf{d}_i$ is expressed by

$$\mathbf{d}_i = [\overline{w}_1, \overline{\theta}_{x1}, \overline{\theta}_{y1}, \overline{w}_2, \overline{\theta}_{x2}, \overline{\theta}_{y2}, \overline{w}_3, \overline{\theta}_{x3}, \overline{\theta}_{y3}, \overline{w}_4, \overline{\theta}_{x4}, \overline{\theta}_{y4}]^{\mathrm{T}} \tag{2.14}$$

where

$$\overline{w}_i = w\Big|_{x_i, y_i} \qquad \overline{\theta}_{xi} = \frac{\partial w}{\partial y}\bigg|_{x_i, y_i} \qquad \overline{\theta}_{yi} = -\frac{\partial w}{\partial x}\bigg|_{x_i, y_i} \tag{2.15}$$

And the displacement field can be expressed as follows

$$\mathbf{d} = \mathbf{H}\mathbf{L}^{\mathrm{T}}\mathbf{X}^{-1}\mathbf{d}_i \qquad i = 1, \ldots, n \tag{2.16}$$

where

$$\mathbf{H}=\begin{bmatrix}1&0&0\\0&-z&0\\0&0&-z\end{bmatrix}\qquad \mathbf{L}=\begin{bmatrix}0&0&0&2&0&0&6x&2y&0&0&6xy&0\\0&0&0&0&0&2&0&0&2x&6y&0&6xy\\0&0&0&0&2&0&0&4x&4y&0&6x^2&6y^2\end{bmatrix} \tag{2.17}$$

$$\mathbf{X}=\begin{bmatrix}1&x_1&y_1&x_1^2&x_1y_1&y_1^2&x_1^3&x_1^2y_1&x_1y_1^2&y_1^3&x_1^3y_1&x_1y_1^3\\1&0&1&0&x_1&2y_1&0&x_1^2&2x_1y_1&3y_1^2&x_1^3&3x_1y_1^2\\0&-1&0&-2x_1&-y_1&0&-3x_1^2&-2x_1y_1&-y_1^2&0&-3x_1^2y_1&-y_1^3\\1&x_2&y_2&x_2^2&x_2y_2&y_2^2&x_2^3&x_2^2y_2&x_2y_2^2&y_2^3&x_2^3y_2&x_2y_2^3\\1&0&1&0&x_2&2y_2&0&x_2^2&2x_2y_2&3y_2^2&x_2^3&3x_2y_2^2\\0&-1&0&-2x_2&-y_2&0&-3x_2^2&-2x_2y_2&-y_2^2&0&-3x_2^2y_2&-y_2^3\\1&x_3&y_3&x_3^2&x_3y_3&y_3^2&x_3^3&x_3^2y_3&x_3y_3^2&y_3^3&x_3^3y_3&x_3y_3^3\\1&0&1&0&x_3&2y_3&0&x_3^2&2x_3y_3&3y_3^2&x_3^3&3x_3y_3^2\\0&-1&0&-2x_3&-y_3&0&-3x_3^2&-2x_3y_3&-y_3^2&0&-3x_3^2y_3&-y_3^3\\1&x_4&y_4&x_4^2&x_4y_4&y_4^2&x_4^3&x_4^2y_4&x_4y_4^2&y_4^3&x_4^3y_4&x_4y_4^3\\1&0&1&0&x_4&2y_4&0&x_4^2&2x_4y_4&3y_4^2&x_4^3&3x_4y_4^2\\0&-1&0&-2x_4&-y_4&0&-3x_4^2&-2x_4y_4&-y_4^2&0&-3x_4^2y_4&-y_4^3\end{bmatrix}$$

3. Piezoelectric constitutive equations

The linear constitutive relations of piezoelectric materials are given as follows

$$\boldsymbol{\sigma}=\mathbf{C}^E\boldsymbol{\varepsilon}-\mathbf{e}^{\mathrm{T}}\mathbf{E}\qquad \mathbf{D}=\mathbf{e}\boldsymbol{\varepsilon}+\boldsymbol{\xi}^s\mathbf{E} \tag{3.1}$$

In the matrix form

$$\begin{bmatrix}\boldsymbol{\sigma}\\\mathbf{D}\end{bmatrix}=\begin{bmatrix}\mathbf{C}^E&-\mathbf{e}^{\mathrm{T}}\\\mathbf{e}&\boldsymbol{\varsigma}^s\end{bmatrix}\begin{bmatrix}\boldsymbol{\varepsilon}\\\mathbf{E}\end{bmatrix} \tag{3.2}$$

where $\boldsymbol{\sigma}$, $\mathbf{D}$, $\boldsymbol{\varepsilon}$, $\mathbf{E}$, $\mathbf{C}^E$, $\mathbf{e}$, $\boldsymbol{\varsigma}^S$ are the stress field, electric flux vector, strain field, electric field vector, elastic constant matrix, piezoelectric coupling constant matrix, and electric coefficient matrix, respectively.

Applying voltage to the element seems similar to applying heat to a bimetallic strip. The voltage Φ_a across the bender element forces the bottom layer to expand, as illustrated in Fig. 3a, while the top layer is contracted.

As a result of these physical phenomena, there is a significant curvature, implying a substantial deflection at the tip while the other end is clamped. Due to the reciprocity effect, the sensor deformation generates a charge across the electrode, collected as a voltage Φ_s through another sensor surface. The equation expresses the applied/perceived electric potential via the actuator or sensor element (Lopes *et al.*, 2000)

$$\phi_z=\Big(\frac{z-0.5h_p}{h}\Big)\phi \tag{3.3}$$

where h, ϕ and $z(z_a,z_s)$ are the thicknesses, maximum electric potentials at the external surfaces of the corresponding piezoelectric elements. The variables $z(z_a,z_s)$ can be obtained as follows

$$\frac{h_p}{2}\leqslant z_a\leqslant\frac{h_p}{2}+h_a\qquad -\frac{h_p}{2}\geqslant z_s\geqslant-\frac{h_p}{2}-h_s \tag{3.4}$$

The assumption for the electric field E remains constant regardless of the thickness of actuator and sensor parts, and the gradient operators are recast as follows

$$E=-\operatorname{grad}\phi=-\frac{\partial\phi_z}{dz}=-B_z\qquad \varphi=-\frac{\phi}{h} \tag{3.5}$$

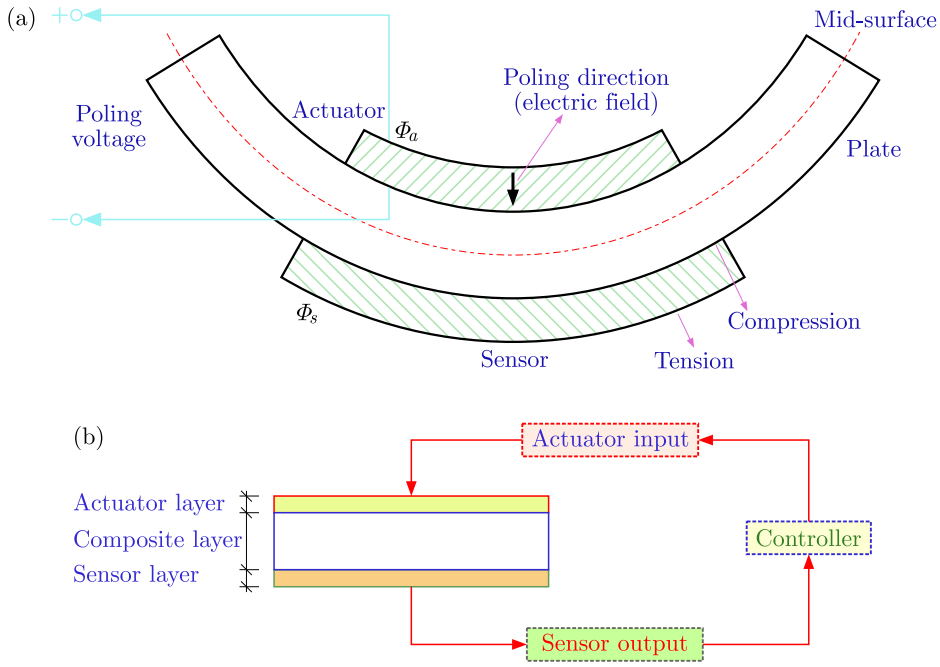

Fig. 3. (a) Curvature of the plate caused by mid-layer and contraction of both sides. (b) A control diagram for the laminate plate with integrated piezoelectric sensors and actuators

However, for implementation of an experiment in this article, the electric field $\mathbf{E}$ is assumed

$$\mathbf{E} = \begin{bmatrix} 0 \\ 0 \\ E_3 \end{bmatrix} \qquad \text{with } \mathbf{B}_z = \begin{bmatrix} 0 \\ 0 \\ \frac{1}{h} \end{bmatrix} \tag{3.6}$$

where h is the thickness of the piezoelectricity material.

With linear piezoelectric materials, the elastic coefficient matrix, piezoelectric stress coefficient matrix, and dielectric coefficient matrix are given by

$$\mathbf{C}^E = \begin{bmatrix} C_{11} & C_{12} & 0 \\ C_{21} & C_{22} & 0 \\ 0 & 0 & C_{33} \end{bmatrix} \qquad \mathbf{e} = \begin{bmatrix} 0 & 0 & 0 \\ 0 & 0 & 0 \\ e_{31} & e_{31} & 0 \end{bmatrix} \qquad \boldsymbol{\xi}^s = \begin{bmatrix} \xi_{11} & 0 & 0 \\ 0 & \xi_{11} & 0 \\ 0 & 0 & \xi_{11} \end{bmatrix} \tag{3.7}$$

4. The governing equations and finite element formulation

A two-dimensional piezoelectric problem in the domain Ω bounded by Γ is considered to be carried out. The governing equations and boundary conditions for linear piezoelectric materials are introduced as follows (Saravanos and Keyliger, 1999)

$$\sigma_{ij,i} + f_j = \rho \ddot{u}_j \qquad \varepsilon_{ij} = \frac{1}{2}(u_{i,j} + u_{j,i}) \qquad D_{i,j} = 0 \qquad E_i = -\phi_{,i} \tag{4.1}$$

By integrating with the boundary conditions

$$\begin{aligned} &\sigma_{ij} n_j = \overline{t}_i \quad \text{on} \quad \Gamma_\sigma \qquad && u_i = \overline{u}_i \quad \text{on} \quad \Gamma_u \\ &\phi = \overline{\phi} \quad \text{on} \quad \Gamma_\phi && D_i n_i = -\overline{q} \quad \text{on} \quad \Gamma_q \end{aligned} \tag{4.2}$$

where σ_{ij} and ε_{ij} denote the stress and strain tensors, respectively. f_j is the body force density, u_j is the mechanical displacement vector, and ρ is the mass density. The electric displacement

vector is D_i, the electric field vector is E_i, and the scalar electric potential field is φ. Summing the kinetic energy, strain energy, dielectric energy, and potential energy of external fields yields the general functional L. The disadvantage of the governing equations of piezoelectric structures is to use the Hamilton principle, written as follows (Lopes etal, 2000; Phung-Van *et al.*, 2013)

$$I = \int_{t1}^{t2} L\, dt = \int_{t1}^{t2} [\delta(T - U + W_e - W_m) + \delta W]\, dt \tag{4.3}$$

where t_1 and t_2 are two random instants. L, T, U and W_e are the general energy functional, kinetic energy, potential energy, and the work done by electrical forces, respectively. The variable W is the mechanical force, being negligible for piezoelectric material. The total potential energy U and kinetic energy T of the composite structure are described as follows

$$U = \frac{1}{2}\int \boldsymbol{\varepsilon}^{\mathrm{T}}\boldsymbol{\sigma}\, dV \qquad T = \frac{1}{2}\int \rho\dot{\mathbf{d}}^{\mathrm{T}}\dot{\mathbf{d}}\, dV \tag{4.4}$$

where $\dot{\mathbf{d}}$ is the differentiation of $\mathbf{d}$ with respect to time, $\mathbf{d}$ is the nodal displacement field, and dV is defined by

$$dV = dV_a + dV_p + dV_s \tag{4.5}$$

Herein, the subscripts a, p and s denote the actuator, plate, and sensor parts, respectively, and dV_a, dV_p and dV_s are given by

$$\begin{aligned} dV_p &= \int_{-h_p/2}^{h_p/2}\int_{-b}^{b}\int_{-a}^{a} dx\, dy\, dz \qquad dV_a = \int_{h_p/2}^{h_p/2+h_a}\int_{-b}^{b}\int_{-a}^{a} dx\, dy\, dz \\ dV_s &= \int_{-h_p/2-h_s}^{-h_p/2}\int_{-b}^{b}\int_{-a}^{a} dx\, dy\, dz \end{aligned} \tag{4.6}$$

The W_e work of electrical forces and the variable W for mechanical forces is illustrated by

$$W_e = \frac{1}{2}\int_V \mathbf{E}^{\mathrm{T}}\mathbf{D}\, dV \qquad W = \int_V \mathbf{q}^{\mathrm{T}}\mathbf{f}_b\, dV + \int_A \mathbf{q}^{\mathrm{T}}\mathbf{f}_A\, dA + \int_A \phi\sigma_q\, dA \tag{4.7}$$

Substituting equation (3.1) into equation (4.4) and equation $(4.7)_1$, we obtain the following

$$U = \frac{1}{2}\int_V \boldsymbol{\varepsilon}^{\mathrm{T}}\mathbf{C}^E\boldsymbol{\varepsilon}\, dV - \frac{1}{2}\int_V \boldsymbol{\varepsilon}^{\mathrm{T}}\mathbf{e}^{\mathrm{T}}\mathbf{E}\, dV \qquad W_e = \frac{1}{2}\int_V \mathbf{E}^{\mathrm{T}}\mathbf{e}\boldsymbol{\varepsilon}\, dV + \frac{1}{2}\int_V \mathbf{E}^{\mathrm{T}}\boldsymbol{\xi}^S\mathbf{E}\, dV \tag{4.8}$$

From equations (4.7) substituted to equation (4.3) one arrives at

$$\int_{t1}^{t2} \delta\mathbf{q}_k^{\mathrm{T}}[\mathbf{M}_{qq}^e\ddot{\mathbf{q}}_k + \mathbf{K}_{qq}^e\mathbf{q}_k + \mathbf{K}_{q\varphi}^e\boldsymbol{\varphi} - \overline{\mathbf{f}}] + \delta\boldsymbol{\varphi}[\mathbf{K}_{\varphi q}^e\mathbf{q}_k + \mathbf{K}_{\varphi\varphi}^e]\boldsymbol{\varphi} + \mathbf{Q}_a]\, dt = 0 \tag{4.9}$$

where

$$\begin{aligned} \mathbf{M}_{qq}^e &= \rho\int_V \mathbf{X}^{-\mathrm{T}}\mathbf{L}_M\mathbf{H}^{\mathrm{T}}\mathbf{H}\mathbf{L}_M^{\mathrm{T}}\mathbf{X}^{-1}\, dV \qquad \mathbf{K}_{qq}^e = \mathbf{X}^{-\mathrm{T}}\int_V z^2\mathbf{L}_K^{\mathrm{T}}\mathbf{D}\mathbf{L}_K\mathbf{X}^{-1}\, dV \\ \mathbf{K}_{q\varphi}^e &= [\mathbf{K}_{\varphi q}^e]^{\mathrm{T}} = -\mathbf{X}^{-\mathrm{T}}\int_V z\mathbf{L}_K^{\mathrm{T}}\mathbf{e}^{\mathrm{T}}B_z\, dV \qquad \mathbf{K}_{\varphi\varphi}^e = -\int_V B_z\boldsymbol{\xi}^S B_z\, dV \\ \overline{\mathbf{f}} &= \int_V \mathbf{f}_b\, dV + \int_A \mathbf{f}_A\, dA \qquad \mathbf{Q}_a = \int_A \sigma_q\, dA \end{aligned} \tag{4.10}$$

Allowing arbitrary variations of dk and φ, from (4.9), we have two equilibrium equations for k-th element in generalized coordinates that are now obtained as follows

$$\mathbf{M}^e_{dd}\ddot{\mathbf{d}}_k + \mathbf{K}^e_{dd}\mathbf{d}_k + \mathbf{K}^e_{\phi\phi}\boldsymbol{\phi} - \overline{\mathbf{f}} = \mathbf{0} \qquad \mathbf{K}^e_{dd}\mathbf{d}_k + \mathbf{K}^e_{\phi\phi}\boldsymbol{\phi} + \mathbf{Q} = \mathbf{0} \tag{4.11}$$

5. Dynamic control

From equation (4.11), the structure system can be rearranged as follows

$$\begin{aligned} &\mathbf{M}_{dd}\ddot{\mathbf{d}} + \mathbf{K}_{dd}\mathbf{d} + \mathbf{K}_{d\phi}\boldsymbol{\phi} - \overline{\mathbf{f}} = \mathbf{0} \qquad \mathbf{K}_{\phi d}\mathbf{d} + \mathbf{K}_{\phi\phi}\boldsymbol{\phi} + \mathbf{Q} = \mathbf{0} \\ &\mathbf{M}_{dd}\ddot{\mathbf{d}} + (\mathbf{K}_{dd} + \mathbf{K}_{d\phi} + \mathbf{K}^{-1}_{\phi\phi} + \mathbf{K}_{\phi d})\mathbf{d} + \mathbf{K}_{d\phi}\boldsymbol{\phi} = \overline{\mathbf{f}} + (\mathbf{K}^{-1}_{\phi\phi} + \mathbf{K}_{\phi d})\mathbf{Q} \end{aligned} \tag{5.1}$$

The resultant control gain is

$$\varphi_a = G_d\varphi_s + G_\nu\varphi'_s \tag{5.2}$$

where G_v and G_d are the velocity and displacement feedback control gains.

The modeling equaton of the system is found as follows

$$M\dot{d} + (C + C_R)\dot{d} + K^*d = F \tag{5.3}$$

where

$$\begin{aligned} &K^* = K_{uu} + G_d[\mathbf{K}_{u\phi}]_s[\mathbf{K}^{-1}_{\phi\phi}]_s[\mathbf{K}_{\phi u}]_s \qquad C = G_v[\mathbf{K}_{u\phi}]_a[\mathbf{K}^{-1}_{\phi\phi}]_s[\mathbf{K}_{\phi u}]_s \\ &C_R = \alpha M + \beta K_{uu} \end{aligned} \tag{5.4}$$

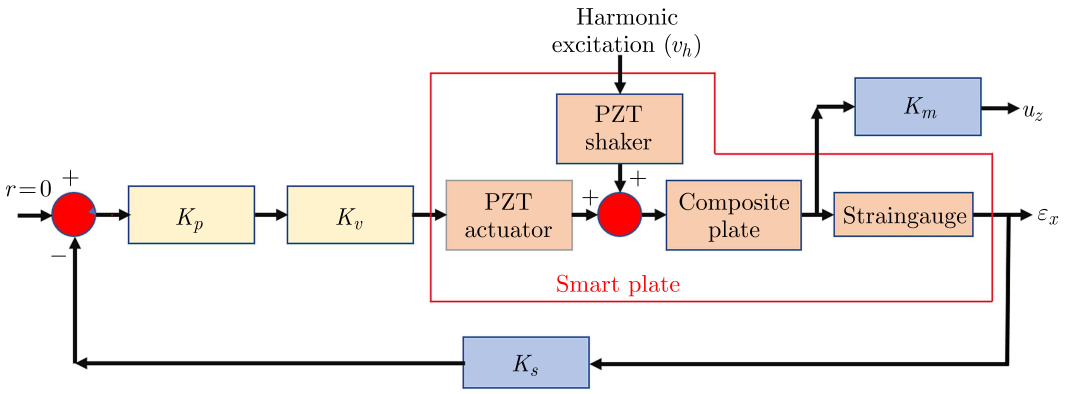

Fig. 4. The control structure of the composite plate by PZT

6. Numerical results

6.1. The first case

Using numerical techniques, the displacement comparison in the first case verifies the proposed method effectiveness. To do this work, the characteristics of piezoelectric material and simply supported (SSSS) of rectangular plates are presented in Table 1 and Fig. 5, respectively. The SSSS boundary conditions are symmetrically bonded with the matching architecture of the piezoelectric actuators and sensors. Furthermore, the effect of piezoelectric patches on the structure static behavior has been investigated.

6.1.1. With steel plate

Table 1. Properties of the steel plate and piezoelectric material

Properties	Piezoelectric material		Steel plate
	sensor	actuator	
Young's modulus E [GPa]	2	69	207
Density ρ [kg/m^3]	1780	7700	7870
Poisson ratio ν	0.3	0.3	0.29
Thickness h [m]	$0.205 \cdot 10^{-3}$	$0.254 \cdot 10^{-3}$	$1 \cdot 10^{-3}$
Piezodielectric ζ^s [F/m]	$1.06 \cdot 10^{1}0$	$1.6 \cdot 10^{8}$	–
Piezoelectric strain e [C/m^2]	0.046	-12.5	–
Capacitance C [F]	$5.2 \cdot 10^{9}$	$6.3 \cdot 10^{7}$	–
Geometry $L_x \times L_y$ [m]	0.1×0.1	0.1×0.1	0.6×0.4

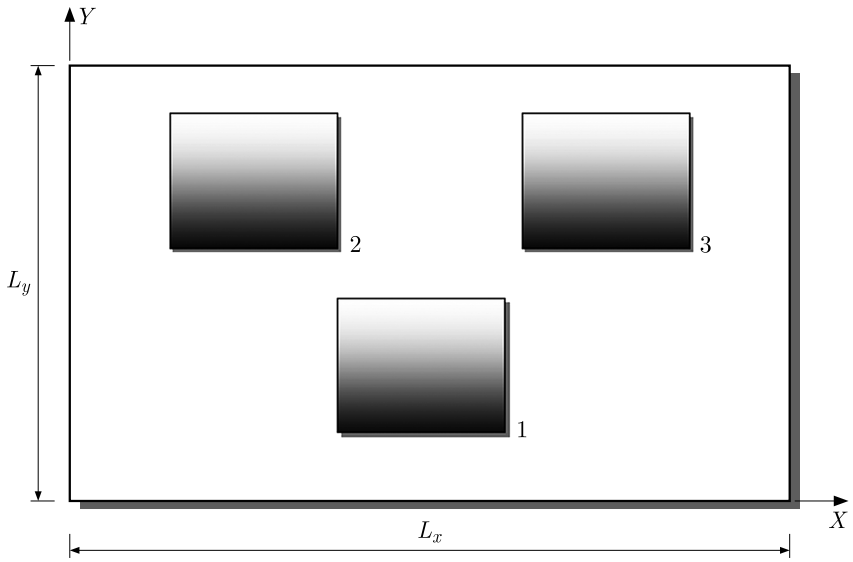

Fig. 5. Piezoelectric actuators and sensors test configuration

The mesh grid (24×16) in the first test is shown in Fig. 6.

Table 2 presents the position of sensors and actuators.

Table 2. Piezoelectric element positions in the x and y dimensions

Properties	Actuators and sensors		
	1	2	3
x	0.25	0.15	0.35
y	0.05	0.25	0.25

Considering the first section, where the position is the plane $y = 0.2$, the displacement graph is shown in Fig. 7.

The total plate displacement amplitude results using the proposed method when a static voltage is applied to the actuator with the magnitude of $\mathbf{\Phi}_a = [-1, 1, 1]$, are shown in Fig. 8.

Table 3 also compares the sensor-generated electric potential results obtained by Abreu *et al.* (2004) and from the proposed method.

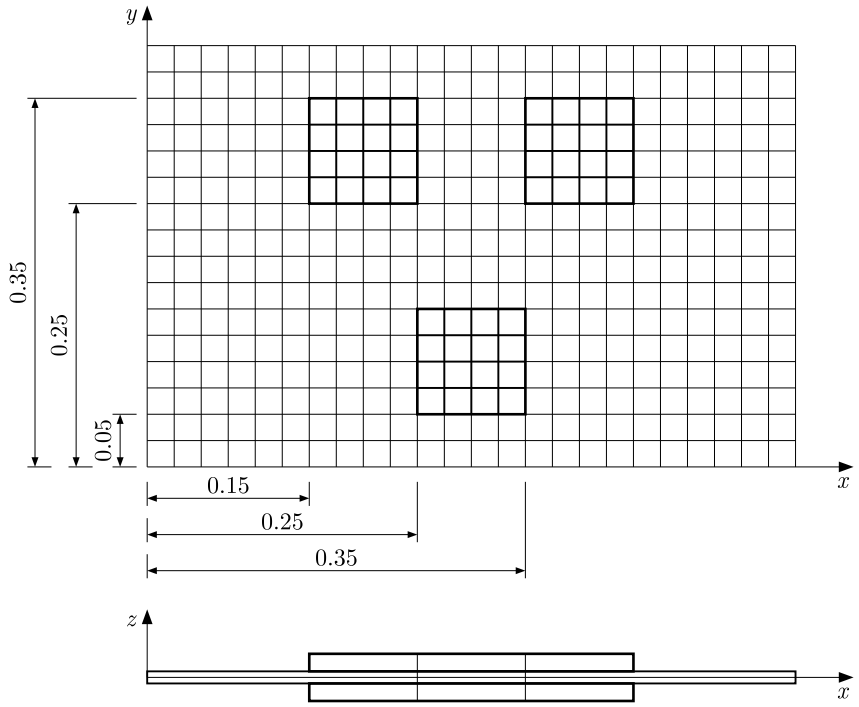

Fig. 6. Mesh grid (24 × 16) and position of actuators and sensors

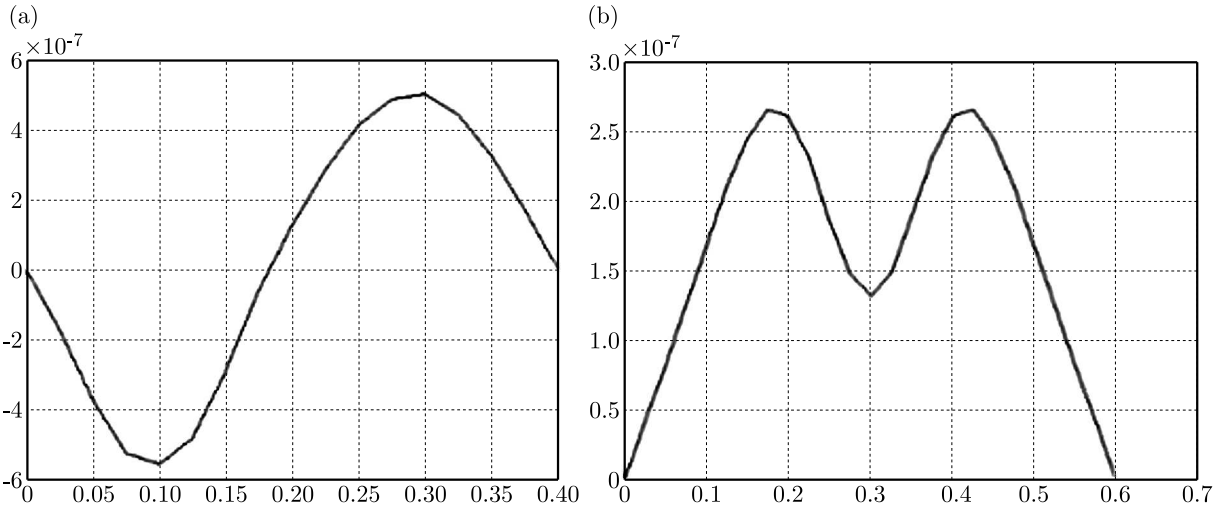

Fig. 7. The displacement graph at the plane $x = x/2$ (left) and $y = y/2$ (right)

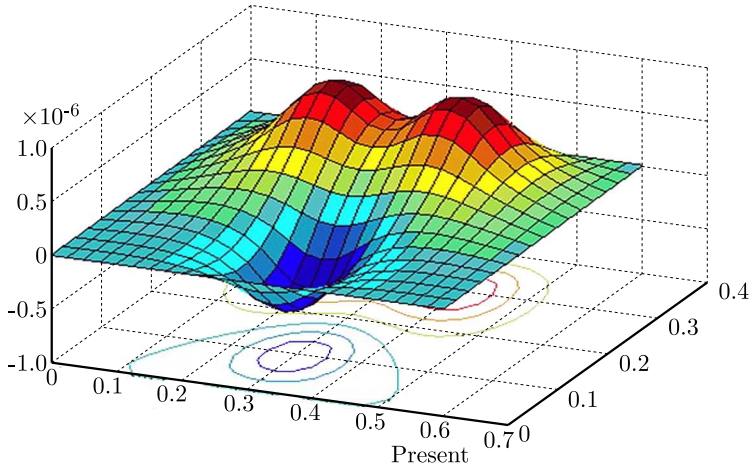

Fig. 8. The total displacement amplitude of the plate

Table 3. The electric potential from sensors

Actuators and sensors	Electric potential V			Err [V]
	Exact solution Abreu *et al.* (2004)	Present	Abreu *et al.* (2004)	
1	+0.0139	+0.0154	+0.0162	0.0015
2	−0.0139	−0.0154	−0.0162	0.0015
3	−0.0139	−0.0154	−0.0162	0.0015

Compared to the exact solution, the errors in Table 3 are small: Err = 0.0015 V, the relative error is about 10% for actuators and sensors. It is declared that the proposed method can be accurately applied to simulate the bending effect (displacement field) in the plate.

As mentioned above, the displacement of the plate is a result of supplying the static voltage to the transmission system. The plate is controlled using the closed loop algorithm to reduce the displacement. The results are illustrated in Fig. 9. The Z-direction displacement in the noncontrollable sensor is bigger than in the controllable one.

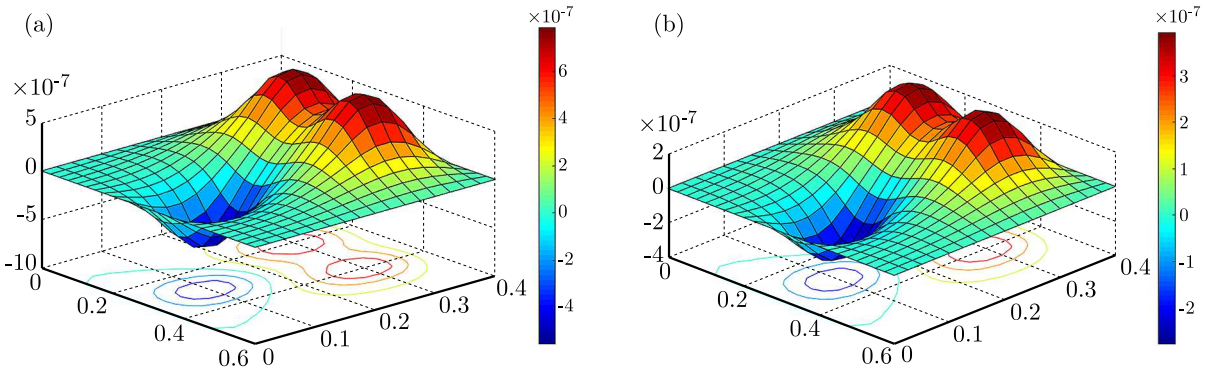

Fig. 9. The total displacement amplitude of the plate: (a) without control, (b) with control

Let us continue to develop the problem with the above material parameters. Apply an evenly distributed load $P = -10\,\mathrm{N}$, place the piezoelectric plate at the center, and control with the input voltages to 10 V, 20 V, 50 V, 100 V and 200 V, and get the results shown in Fig. 10.

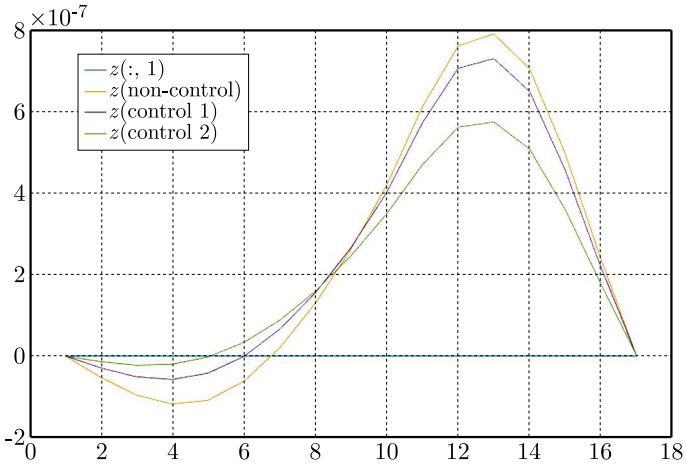

Fig. 10. The displacement graph at the plane $y/2$

The plate displacement decreases over time when other values are kept constant and the voltage is gradually increased. Combined with active control of the plate, the amplitudes of

vibrations decrease progressively over time, and the speed of extinguishing the vibrations is faster than without control. The obtained results are shown in Figs. 11 and 12.

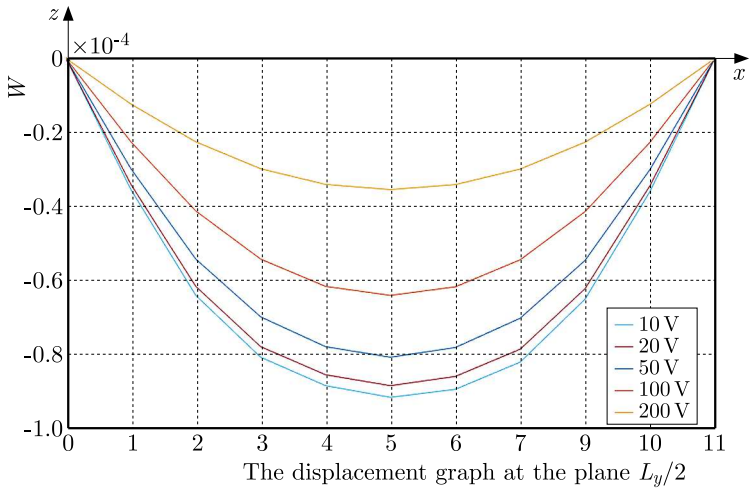

Fig. 11. The displacement graph at the plane $y/2$

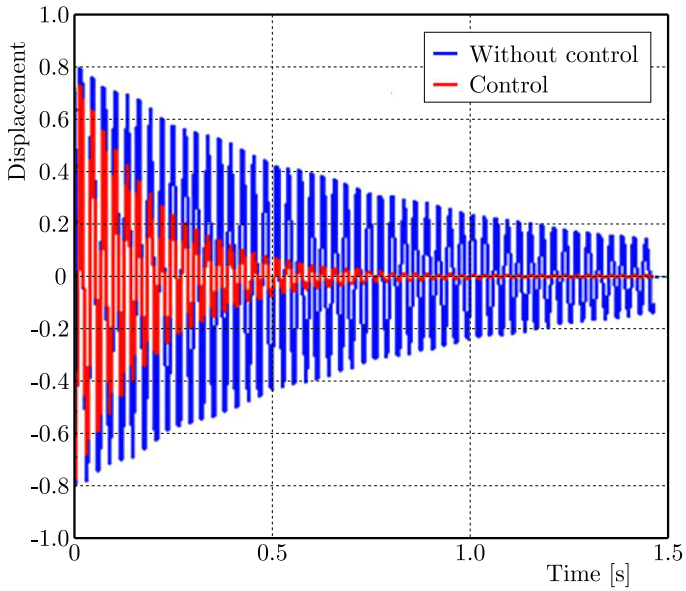

Fig. 12. Comparison of the displacement of the composite plate with control and without control

6.1.2. Changing the composite layers for the plate

The material is a carbon/epoxy composite with a stacking sequence [0/90] s. The properties are listed in Table 4. This composite laminate plate has length $a = 0.38$ m, width $b = 0.3$ m, thickness $t_p = 1.5876$ mm. The PZT G-1195 piezoelectric actuator has Young's modulus $E_{pe} = 63$ GPa, Poisson's ratio $v_{pe} = 0.3$, density $\rho_{pe} = 7600\,\mathrm{kg/m^3}$, piezoelectric constant $\zeta^s = 1.9 \cdot 10^{-10}$ V/m, and thickness $t_{pe} = 0.15876$ mm (Dileep *et al.*, 2017). Through parametric research, the influence of the actuator size and position on the composite plate deflection and deformation shape when activated by the surface-bonded piezoelectric actuator is evaluated.

As shown in Fig. 13, the plate displacement generated relative to PZT decreases linearly as the number of layers increases.

Table 4. Properties of carbon/epoxy material

Longitudinal module E_1 [GPa]	Transverse modulus E_2 [GPa]	Shear modulus G_{12} [GPa]	Poisson's ratio	
			ν_{12}	ν_{21}
108	10.3	7.13	0.28	0.28

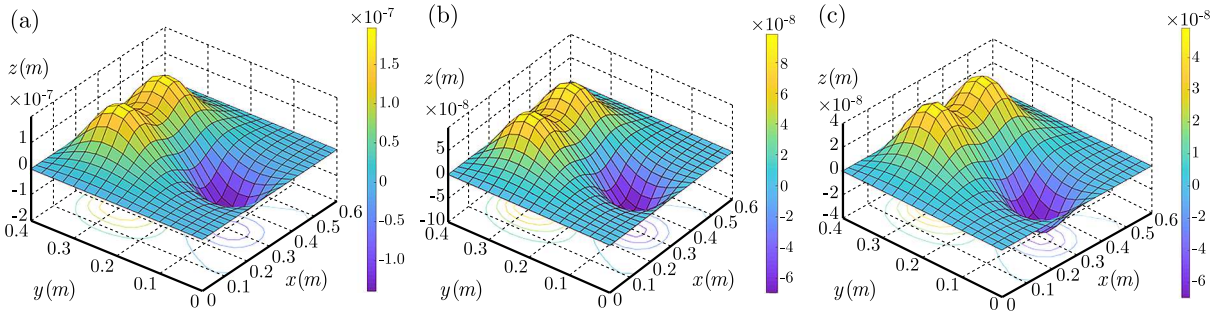

Fig. 13. The total displacement amplitude of the plate with 2-layer (left), 4-layer (between), and 8-layer (right)

When changing the fiber direction of an 8-layer plate, in the case of the $[75, -75]$ s plate arrangement, the best ability to resist displacement caused by the PZT plates is shown in Fig. 14.

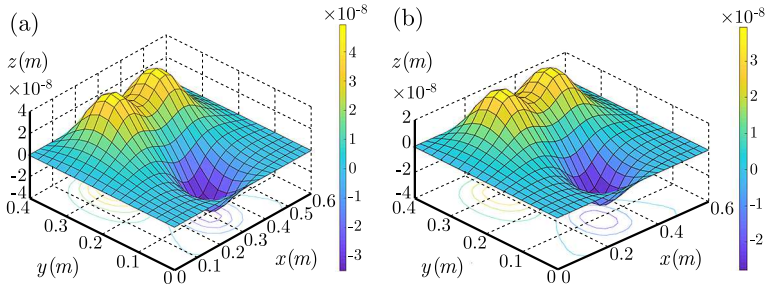

Fig. 14. The total displacement amplitude of the 8-layer composite plate with the fiber direction $[30, 60]$ s (left) and $[75, -75]$ s (right)

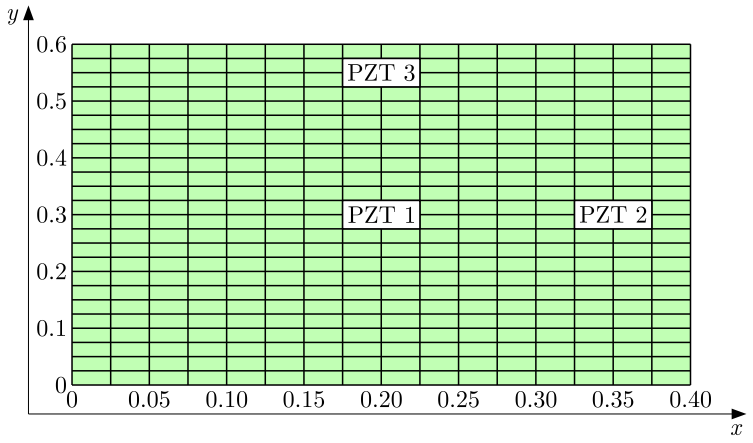

Fig. 15. Mesh model of the composite plate and the positions of 3 PZT patches

The actuators are placed at various locations to study their capability of controlling the plate deflection shape. In this case, the piezoelectric actuators are surface bonded at the plate central, right, and top regions, respectively, as shown in Fig. 15. Those are three typical positions chosen arbitrarily to demonstrate the effect of actuator position on the deflection.

Table 5. Piezoelectric element central positions in x and y dimensions

Properties	Actuators and sensors		
	1	2	3
x	0.2	0.35	0.2
y	0.3	0.3	0.55

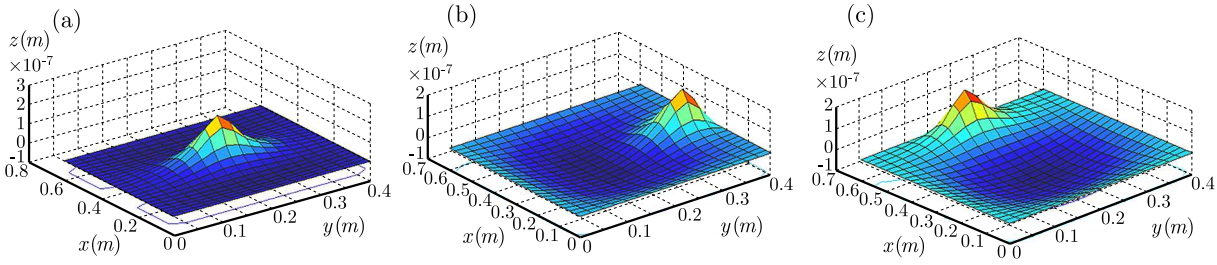

Fig. 16. Displacement of the composite plate with the PZT patch positioned at the center (left), x-axis (between), and y-axis (right)

Table 6. Comparison of the maximum displacement of the composite plate induced by PZT patches at three different positions

Positions	W [mm]
1	−0.2358
2	−0.0849
3	−0.0691

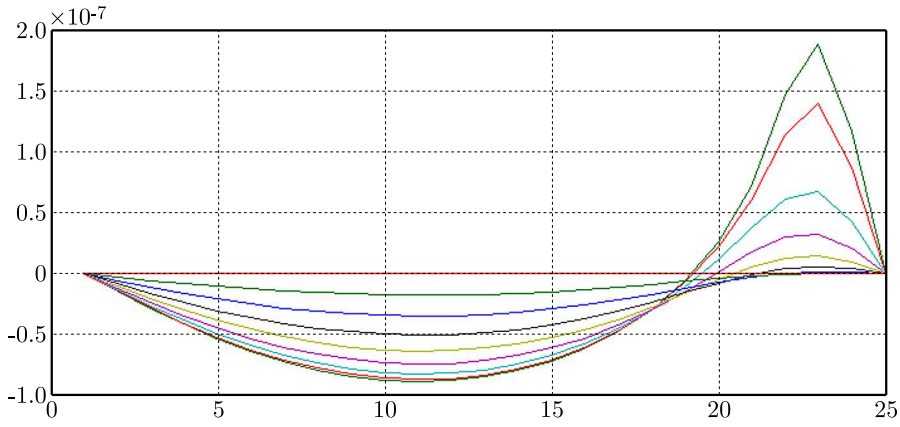

Fig. 17. The displacement graph at the plane $x/2$

When the position of the PZT piece on the composite plate changes, the displacement also changes. The PZT pieces placed closer to the boundary edges will gradually decrease the displacements.

If the composite panel is rectangular, PZT panels placed near the edge along the width direction will have smaller displacements than PZT panels placed at the edge along the length of the panel.

Based on Fig. 17, the torque generated deforms the composite panel where the PZT panel is placed and in the opposite direction in the surrounding area.

6.2. The second case

In this simulation, the proposed algorithm is investigated to control the diving board in diving sports. This article aims to show that the diving board can be safe in the case of overload and help improve athletes' performance before touching the swimming pool surface. The physical parameters of the diving board are 2.5 m×0.4 ×0.01 m for the composite 4-layers [75°/ − 75°/ −75°/75°] and [30°/60°/60°/30°] (shown as Fig. 18). The control diagram is shown in Fig. 3b.

Fig. 18. The model of the diving board (desired scenario)

With diving board composite 4-layers [75°/ − 75°/ − 75°/75°] and [30°/60°/60°/30°], the piezoelectric ceramic (PZT 1V) is stuck in the diving board, as seen in Fig. 19.

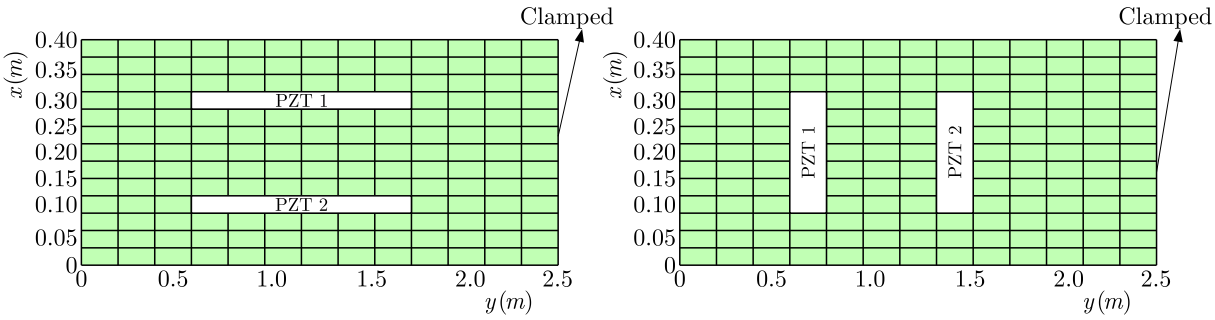

Fig. 19. The position of PZT: scenario 1 (left) and scenario 2 (right)

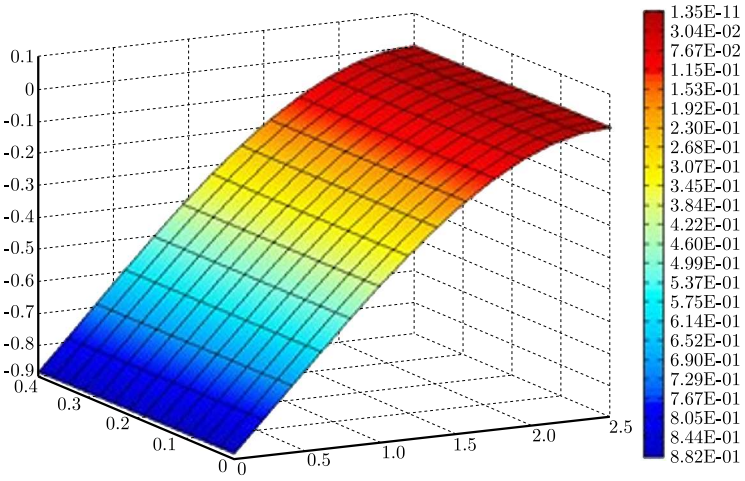

Fig. 20. The displacement (with m unit) of the diving board in non-controllable

The simulation results are found from two scenarios displayed in Figs. 21 and 22 with the composite 4-layers $[75°/-75°/-75°/75°]$ and $[30°/60°/60°/30°]$.

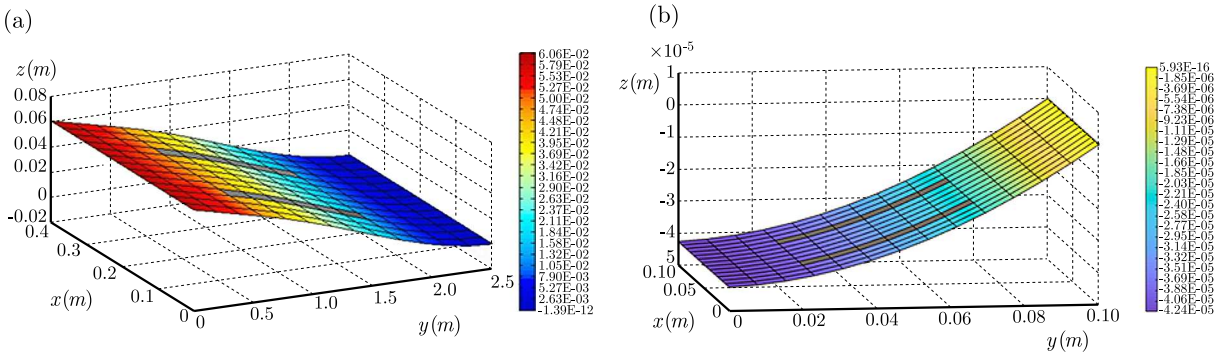

Fig. 21. The displacement of a controlled diving board for scenario 1: fiber direction $[75, -75]$ s (left), fiber direction $[30, 60]$ s (right)

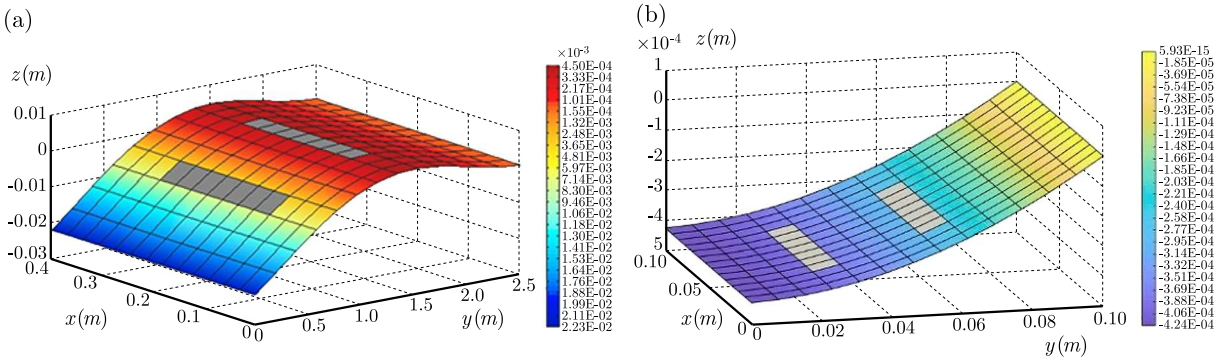

Fig. 22. The displacement of a controlled diving board in scenario 2: fiber direction $[75, -75]$ s (left), fiber direction $[30, 60]$ s (right)

Table 7. Piezoelectric element positions in x and y dimensions

Direction of fibers	Maximum displacement [m]		
	Non-controllable	Scenario 1	Scenario 2
$[75°/-75°/-75°/75°]$	0.8	0.0606	0.0223
$[30°/60°/60°/30°]$	0.8	0.0424	0.0424

The control method backs the diving board approximately to the initial position. Therefore, the displacement of the z-axis of the diving board is narrowed down. Although the displacement of scenario 2 is less than that of scenario 1, the shape of the diving board after controlling scenario 1 is nearly close to the desired scenario. The input voltage controls the desired displacement; therefore, an athlete performs well when turning on the thrust assist bar.

7. Conclusion

- In this article, the deformed shape of the plate bonded to piezoelectric actuators and sensors is investigated by the finite element method (FEM). Based on the Kirchhoff plate model, the FE (finite element) formula was developed for smart composite structures with piezoelectric materials. The modeling technique combining FEM and LQR algorithms was proposed. By analyzing and evaluating the results obtained from the two cases, the effectiveness of computation and application was presented.

- In the first case, a rectangular piezoelectric actuator with symmetrically bonded three sensors is considered. The results are analyzed, errors estimated and compared with other methods and reliable analytical solutions.
- In the second case, the piezoactuator of the injector is considered. From the obtained results, it can be said that the deformed shape of piezoactuators can be computed accurately by FEM. Furthermore, the obtained results also showed that the displacement at the center of the piezoactuator in the injector has a linear relation with the voltage level. These results help the understanding the coupling effects of mechanical and electric properties of piezoelectric actuators and sensors for applications. Besides, the results present the performance of active control LQR and behavior of the actuator modules of the injector in a common system. The convergence rate of the energy norm versus the degree of freedom is reliable.

References

1. Abreu G.L.C.M. de, Ribeiro J.F., Steffen V. Jr., 2004, Finite element modeling of a plate with localized piezoelectric sensors and actuators, *Journal of the Brazilian Society of Mechanical Sciences and Engineering*, **26**, 2, 117-128
2. Adriaens H.J.M.T.S., De Koning W.L., Banning R., 2000, Modeling piezoelectric actuators, *IEEE/ASME Transactions on Mechatronics*, **5**, 4, 331-341
3. Bailey T., Hubbard J.E., 1985, Distributed piezoelectric-polymer active vibration control of a cantilever beam, *Journal of Guidance, Control, and Dynamics*, **8**, 5, 605-611
4. Benjeddou A., Trindade M.A., Ohayon R., 2000, Piezoelectric actuation mechanisms for intelligent sandwich structures, *Smart Materials and Structures*, **9**, 3, 328-335
5. Bhalla S., Moharana S., Talakokula V., Kaur N., 2017, *Piezoelectric Materials: Applications in SHM, Energy Harvesting and Biomechanic*, Wiley
6. Cao X., Tanner G., Chronopoulos D., 2020, Active vibration control of thin constrained composite damping plates with double piezoelectric layers, *Wave Motion*, **92**, 102423
7. Chen L., Xue J., Pan S., Chang L., 2020, Study on cantilever piezoelectric energy harvester with tunable function, *Smart Materials and Structures*, **29**, 7, 075001
8. Chen W., Liu Y., Liu Y., Tian X., Shan X., Wang L., 2018, Design and experimental evaluation of a novel stepping linear piezoelectric actuator, *Sensors and Actuators A: Physical*, **276**, 259-266
9. Chen X., Su C.-Y., Li Z., Yang F., 2016, Design of implementable adaptive control for micro/nano positioning system driven by piezoelectric actuator, *IEEE Transactions on Industrial Electronics*, **63**, 10, 6471-6481
10. Crawley E.F., de Luis J., 1987, Use of piezoelectric actuators as elements of intelligent structures, *AIAA Journal*, **25**, 10, 1373-1385
11. Dileep K.K., Subba Rao V.V., 2017, Vibration control of rectangular cross-ply FRP plates using PZT materials, *Journal of Engineering Science and Technology*, **12**, 12, 3398-3411
12. Dimitriadis E.K., Fuller C.R., Rogers C.A., 1991, Piezoelectric actuators for distributed vibration excitation of thin plates, *Journal of Vibration and Acoustics*, **113**, 1, 100-107
13. Gohery S., Mozafari F., Moslemi N., Mouloodi S., Alebrahim R., *et al.*, 2022, Static and dynamic deformation response of smart laminated composite plates induced by inclined piezoelectric actuators, *Journal of Composite Materials*, **56**, 21, 3269-3293
14. Her S.-C., Chen H.-Y., 2022, Vibration excitation and suppression of a composite laminate plate using piezoelectric actuators, *Materials*, **15**, 6, 2027

15. Hoa P.Q., Van T.T., Dat P.T., Hau D.T., Ha N.V., *et al.*, 2018, Static and free vibration analyses of laminated composite shells by cell-based smoothed discrete shear gap method (CS--DSG3) using three-node triangular elements, *Vietnam Journal of Mechanics*, **40**, 1, 89-103

16. Huang G.L., Sun C.T., 2006, The dynamic behaviour of a piezoelectric actuator bonded to an anisotropic elastic medium, *International Journal of Solids and Structures*, **43**, 5, 1291-1307

17. Jafferis N.T., Lok M., Winey N., Wei G.-Y., Wood R.J., 2016, Multilayer laminated piezoelectric bending actuators: design and manufacturing for optimum power density and efficiency, *Smart Materials and Structures*, **25**, 5, 055033

18. Karegar M., Bidgoli M.R., Mazaheri H., 2021, Smart control and seismic analysis of concrete frames with piezoelectric layer based on mathematical modelling and numerical method, *Structures*, **32**, 1171-1179

19. Latrache M., Menasri N., 2022, Active control vibration of a smart composite plate for various boundary conditions, *Turkish Journal of Computer and Mathematics Education (TURCOMAT)*, **13**, 2, 671-688

20. Lopes V. Jr., Pereira J.A., Inman D.J., 2000, Structural FRF acquisition via electric impedance measurement applied to damage location, [In:] *IMAC XVIII. Proceedings of IMAC--XVIII: A Conference on Structural Dynamics*, San Antonio, USA, 41, 1549-1555

21. Lumentut M.F., Howard I.M., 2014, Electromechanical finite element modelling for dynamic analysis of a cantilevered piezoelectric energy harvester with tip mass offset under base excitations, *Smart Materials and Structures*, **23**, 9, 095037

22. Luo Q., Tong L., 2006, High-precision shape control of plates using orthotropic piezoelectric actuators, *Finite Elements in Analysis and Design*, **42**, 11, 1009-1020

23. Moretti M., Silva E.C.N., 2019, Topology optimization of piezoelectric bi-material actuators with velocity feedback control, *Frontiers of Mechanical Engineering*, **14**, 2, 190-200

24. Phung-Van P., Nguyen-Thoi T., Le-Dinh T., Nguyen-Xuan H., 2013, Static and free vibration analyses and dynamic control of composite plates integrated with piezoelectric sensors and actuators by the cell-based smoothed discrete shear gap method (CS-FEM-DSG3), *Smart Materials and Structures*, **22**, 9, 095026

25. Reddy J.N., 1999, On laminated composite plates with integrated sensors and actuators, *Engineering Structures*, **21**, 7, 568-593

26. Saravanos D.A., Heyliger P.R., 1999, Mechanics and computational models for laminated piezoelectric beams, plates, and shells, *Applied Mechanics Reviews*, **52**, 10, 305-320

27. Trojanowski R., Wiciak J., 2020, Impact of the size of the sensor part on sensor-actuator efficiency, *Journal of Theoretical and Applied Mechanics*, **58**, 2, 391-401

28. Uchino K., 1986, Electrostrictive actuators: materials and application, *American Ceramic Society Bulletin*, **65**, 4, 647-652

29. Uchino K. (Edit.), 2010, *Advanced Piezoelectric Materials: Science and Technology*, Woodhead Publishing Limited

30. Wang X., Shen Y., 1998, On the characterization of piezoelectric actuators attached to structures, *Smart Materials and Structures*, **7**, 3, 389-395

31. Wei H., Wang H., Xia Y., Cui D., Shi Y., *et al.*, 2018, An overview of lead-free piezoelectric materials and devices, *Journal of Materials Chemistry C*, **6**, 46, 12446-12467

Manuscript received April 8, 2024; accepted for publication October 18, 2024